An ultrahigh mass-loading integrated high coulombic efficiency Si–graphite electrode for high-energy-density lithium ion batteries†

Shu Zhang,‡[a] Yi Zhu,‡[a] Xiandi Zhang,[a] Fanglin Hu,[a] Wengao Zhao,*[b] Jianxuan Du,[b] Shuyue Xue,[a] Peng Li [iD] *[a] and Yu-Jia Zeng [iD] *[c]

Nowadays, researchers are increasingly interested in silicon-based anode active materials for lithium-ion batteries, which could meet the ever-increasing demand for high energy density owing to their satisfactory theoretical capacity ($\sim$4200 mA h g^{-1}). However, replacing graphite with silicon is still insurmountable due to unsatisfactory coulombic efficiency (ICE), low electrode loading, and insufficient areal capacity. In this study, a silicon–graphite electrode is developed to overcome these limitations, providing excellent experimental data, *i.e.*, a promising ICE of 88%, an ultrahigh areal capacity of 7.4 mA h cm^{-2} and an impressive loading level of $\sim$20 mg cm^{-2}. Additionally, special characterization, such as stress simulation and friction tests, further verified the stability of the rationally designed electrode. Such satisfactory performance is ascribed to the enhanced conductivity induced by carbon nanotube insertion and boron modification, a reliable volume buffer effect originating from the graphite framework, and ion transport promotion and side reaction prevention induced by lithium-rich binder engineering.

Introduction

Owing to the popularity of portable electronics, hybrid electric vehicles, and other energy storage systems, high energy density and low-cost lithium-ion batteries (LIBs) have been playing an increasingly important role.[1] For a long time, graphite has been the most conventional anode active material because of its low potential and good electrochemical as well as physical stability. However, its poor theoretical capacity (372 mA h g^{-1}) cannot

[a]Department of Chemical Engineering, Shandong University of Technology, 255000, China. E-mail: Peng.Li.UPC@hotmail.com

[b]Institute of Nanotechnology, Karlsruhe Institute of Technology (KIT), 76344 Eggenstein-Leopoldshafen, Germany. E-mail: wengao.zhao@kit.edu

[c]Key Laboratory of Optoelectronic Devices and Systems of Ministry of Education and Guangdong Province, College of Physics and Optoelectronic Engineering, Shenzhen University, 518060, China. E-mail: yjzeng@szu.edu.cn

meet the requirements of next-generation high-energy-density LIBs.[2] Therefore, advanced electrodes with high lithium storage capability have become the research focus, in which attempts have been made to achieve high energy and power density.[3] To date, active materials with high theoretical capacities, such as silicon (4200 mA h g^{-1}),[4] tin (991 mA h g^{-1}),[5] and germanium (1624 mA h g^{-1}),[6] have been proposed as alternatives to graphite. Among them, silicon has excellent theoretical capacity, appropriate operating potential, and natural abundance, and is considered one of the most promising anode materials for LIBs.[7] Despite the significant improvement achieved in the last few years, replacing graphite with silicon is still challenging due to tedious silicon optimization, unsatisfactory coulombic efficiency, low electrode loading level, and insufficient areal capacity. Ge *et al.* proposed a HF assisted intractable Ag$^+$ etching strategy for porosity construction. Boron doping was then performed at a high temperature of 900 °C.[8] Yi *et al.* enhanced the rate performance of a silicon/carbon composite by B$_2$O$_3$ boron doping at 950 °C, and the electrode loading level was only 1.2 mg cm^{-2}.[9] Wang *et al.* also successfully optimized porous silicon *via* high thermal energy consumption at 950 °C, which could provide an insufficient areal capacity of 1.9 mA h cm^{-2} at *ca.* 1.0 mg cm^{-2}.[10] In addition, in previous studies, the unsatisfactory ICE was another shortcoming, which cannot be neglected especially for practical applications. The most widely used method for eliminating the irreversible capacity loss during the first cycle is prelithiation through lithium powder casting,[11] metallic lithium foil pressing,[12] or electrochemical precycling.[13] Nevertheless, such prelithiation approaches generally involve high costs or require complex operations. Therefore, several attempts have been made to increase the ICE, such as interfacial incorporation of metal nanocrystals,[14] dense silicon,[15] or alumina atomic layers.[16] However, crystal coating and atomic deposition are either time-consuming or relatively hard to control. Recently, binder engineering *via* molecular structural modification or mutual combination has emerged as a facile method for ICE enhancement, which might also be effective for prelithiation

elimination.[17] Compared with sp[3] hybridization, carbon atoms in CNTs mostly adopt sp[2] hybridization, which has a larger s orbital component and higher modulus. The p orbitals can form highly delocalized large π bonds outside the tube through overlapping each other, ensuring a significant conjugation effect and excellent electrical conductivity.[18,19] Besides, their unique nanotube structure guarantees facile insertion into the pores of silicon, which makes it possible to enhance the conductivity of silicon from the inside as well as the outside. The advantages of graphite, such as abundant reserves and impressive stability, should not be ignored. When adding a small amount of silicon active materials into graphite, the graphite matrix could act as a tough buffer framework; it could effectively mitigate the structural stress of silicon upon repeated lithiation and delithiation.

Herein, we rationally design a high-loading CNT,B-codoped silicon electrode upon waste heat assistance and Li-rich binder engineering for high-energy-density Li-ion batteries. The obtained silicon based electrode has two main parts, i.e., CNT, boron co-modified porous silicon (10 wt%) and graphite buffer matrix (90 wt%). In the silicon part, the CNT content is 15 wt% and the boron content is 4.9 at%. The boron-doped porous silicon taking advantage of magnesium reduction as well as its intensive waste heat for porosity construction and boron doping at relatively low temperature (525 °C) could provide impressive reversible capacity (2585 mA h g^{-1}) and good cycling stability for over 200 cycles. After incorporating with reliable graphite, the obtained nano/microstructured silicon–graphite composite achieves a remarkable areal capacity of 7.4 mA h cm^{-2} at an ultrahigh loading level of ∼20 mg cm^{-2}. Notably, satisfactory ICE and prelithiation exclusion can be realized simultaneously via lithium-rich binder engineering, implying its promising application potential.

Experimental section

Materials and methods

Synthesis of the low temperature boron-doped nano/microstructured silicon (LB-Si/CT). In a typical procedure, silicon monoxide powder (1.0 g) and B$_2$O$_3$ (0.25 g) were thoroughly ground with magnesium powder (3.6 g), and the mixture was subsequently annealed at 525 °C for 5 h under an argon atmosphere. The porosity construction and boron modification were realized simultaneously. Then, 5% HF solution was very carefully used to remove the small amount of residual SiO$_2$ on the surface of porous silicon (LB-Si). The LB-Si/CT composite was obtained after incorporating LB-Si with CNTs (15 wt%) using a ball mill at a frequency of 15 Hz. For comparison, a Si–B$_2$O$_3$ mixture was prepared at the same annealing temperature followed by the same washing procedure to confirm the effectiveness of low-temperature boron doping.

Preparation of the modified silicon–graphite composite (LB-Si/CT@G). To prepare the nano/micro-structured silicon–graphite composite, LB-Si/CT (10.0 wt%) was thoroughly blended with graphite using a SPEX mill for 1 h. In addition, bare silicon–graphite (Si–G) and pure graphite electrodes were examined comparatively.

Lithium-rich binder engineering. The enhanced binder was obtained through a facile and carefully controlled neutralization reaction between lithium hydroxide solution and polyacrylic acid solution. The neutralization process was carried out slowly during intensive stirring.

Characterization of the samples

The as-prepared products were characterized using an XRD (RINT-2000, Rigaku) instrument with Cu Kα radiation ($\lambda = 1.518$ Å). The porosity microstructure of the prepared materials was examined using an Autosorb-1 (Quantachrome) instrument. A scanning electron microscopy (JSM-6400, JEOL) device and a transmission electron microscopy (JEM-2010, JEOL) apparatus were used to investigate the microstructure of the prepared materials. Furthermore, Raman analysis was performed using an inVia (Renishaw) Raman spectrometer to determine the crystallinity of the as-prepared materials. The chemical composition and elemental states were investigated using a PHI 5000 VersaProbe XPS instrument. A friction test was further conducted on a Multifunctional Friction Testing Machine (MFT-5000, Rtec, USA).

Electrochemical measurements

The LB-Si/CT anode was prepared by coating a slurry comprising the active material, super P, and PAA binder (8 : 1 : 1 w/w/w) onto a copper foil current collector. After drying at 100 °C, the electrode was assembled into a CR2032 coin cell under an argon atmosphere using lithium foil as the counter electrode and a polypropylene membrane as the separator. For the blended electrodes, LB-Si/CT@G was cast with 2% super P and 5% PAA or LiPAA binder. In addition, 1 M LiPF$_6$ in a 1 : 1 (v/v) ethylene carbonate and diethyl carbonate with 10 wt% fluoroethylene carbonate solution was used as the electrolyte. For the GITT study, the as-assembled coin cells were tested at a pulse current of 100 mA g^{-1} for 30 min alternating with 2 h rest intervals. Cyclic voltammetry was performed using a VMP3 (BioLogic) electrochemical station.

Results and discussion

The strategy of silicon preparation includes facile low-temperature boron penetration taking advantage of intensive waste heat induced by magnesium reduction and CNT insertion through an economical solid-state process. Bulk silicon monoxide and boron oxide are selected as the precursors. After magnesium alloying, boron modified Mg$_2$Si and MgO could be obtained. Then sufficient oxidation is conducted, transforming the Mg$_2$Si into Si and MgO. Through acid etching, useless MgO is removed, leaving porous boron-modified silicon (LB-Si). As silicon is a kind of semiconductor, the conductivity is not high enough for ideal lithium-ion batteries. Thus, after careful comparison, commercial carbon nanotubes are selected to enhance the conductivity of silicon based active materials. After sufficient ball milling, the carbon nanotubes could be rationally inserted into pores of silicon, as expected. The obtained nano/microsystem integrated reasonable porosity construction,

heteroatom penetration, and nanoblock engineering. X-ray diffraction (XRD) patterns were obtained to determine the composition of all intermediate products. After the slow redox reaction, the typical peaks of Mg_2Si and MgO (JCPDS card no 36-0773 and 89-4248, respectively) could be observed in the XRD pattern in Fig. 1a, which indicates a thorough transformation of the precursor.[20] After CNT insertion, LB-Si/CT was collected, and intensive peaks indexed to those of face-centered cubic crystalline Si (JCPDS card no 27-1402) can be clearly observed.[12]

To further analyze the composition of the obtained products, Raman spectra were attained (Fig. 1b). The peaks at around 514 cm^{-1} in the spectra of LB-Si and LB-Si/CT are ascribed to the Raman phonon vibration of silicon, and the two peaks at ~1348 and 1588 cm^{-1} correspond to the D and G bands of carbon, confirming the effective integration of CNTs in the composite.[21] The successful low-temperature boron doping is further revealed by X-ray spectroscopy (XPS) investigation (Fig. 1c). No boron signal was detected in the spectrum of the Si–B_2O_3 comparative sample, while two typical peaks, i.e., the B–B and B–Si peaks (188.0 and 187.1 eV, respectively), can be easily identified in the profile of LB-Si after peak-splitting.[22] The boron content of LB-Si/CT was calculated to be 4.9 at%. Additionally, Fig. 1d presents the N_2 adsorption/desorption isotherms of the as-prepared products. The Brunauer–Emmett–Teller surface area of LB-Si/CT was as high as 95.2 m^2 g^{-1}, and the pore-size

distribution of LB-Si/CT, calculated using the Barrett–Joyner–Halenda method, is mainly centered at 18 nm. Nonetheless, the SiO precursor presented nearly no porosity, and its low surface area (0.9 m^2 g^{-1}) is detrimental to ion penetration and lithium storage.[23]

The microstructural features and typical morphology of the as-prepared samples were further investigated using scanning electron microscopy. Compared with the compact SiO precursor (Fig. 2a), LB-Si shows an unequivocal nano-microporous structure (Fig. 2b–d), in which the abundant nanopores are beneficial to sufficient volume change accommodation and fast ion transportation. Carbon nanotubes are tightly wedged into the porous silicon thorough mechanical milling (Fig. 2e), which is clearly shown in Fig. 2f, optimizing the synergistic effect of high-capacity silicon and well-conductive CNTs. Fig. 2g presents the first nine cyclic voltammetry (CV) cycles of LB-Si/CT in the range of 0.01-1.5 V at a scan rate of 0.1 mV s^{-1}. The peak at ~0.1 V observed in the cathodic process during the first cycle is related to the formation of amorphous Li_xSi.[24] The two anodic peaks at 0.36 and 0.52 V are attributed to the two-step phase transition of α-Li_xSi into amorphous silicon (α-Si).[25] Many important parameters of lithium-ion batteries, e.g., lithiation/delithiation voltage, specific capacity and initial coulombic efficiency, could be obtained in the first cycle. As can be seen in Fig. S1,† there is a long and stable lithiation process at
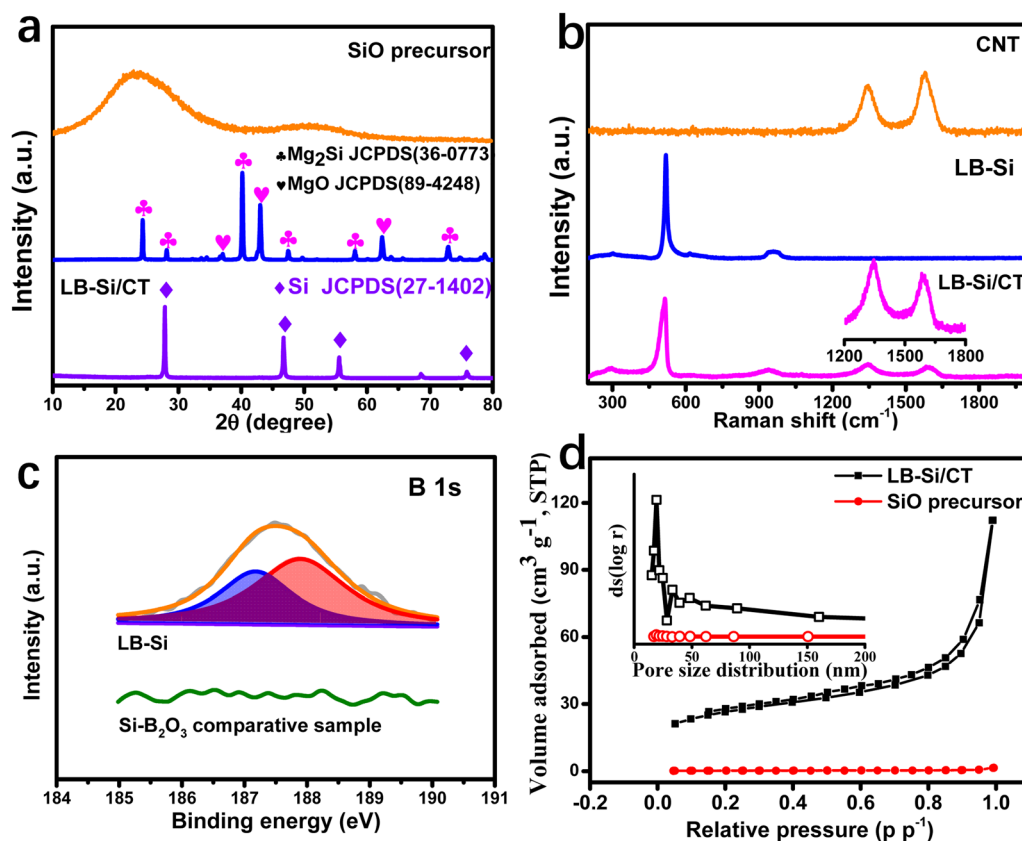

Fig. 1 (a) X-ray diffraction patterns of the SiO precursor, Mg_2Si/MgO intermediates, and LB-Si/CT. (b) Raman spectra of carbon nanotubes (CNTs), low temperature boron-doped porous silicon (LB-Si), and LB-Si/CT. (c) B 1s X-ray photoelectron spectroscopy profile of LB-Si and Si–B_2O_3. (d) N_2 adsorption/desorption isotherms and pore-size distribution of LB-Si/CT and the SiO precursor.
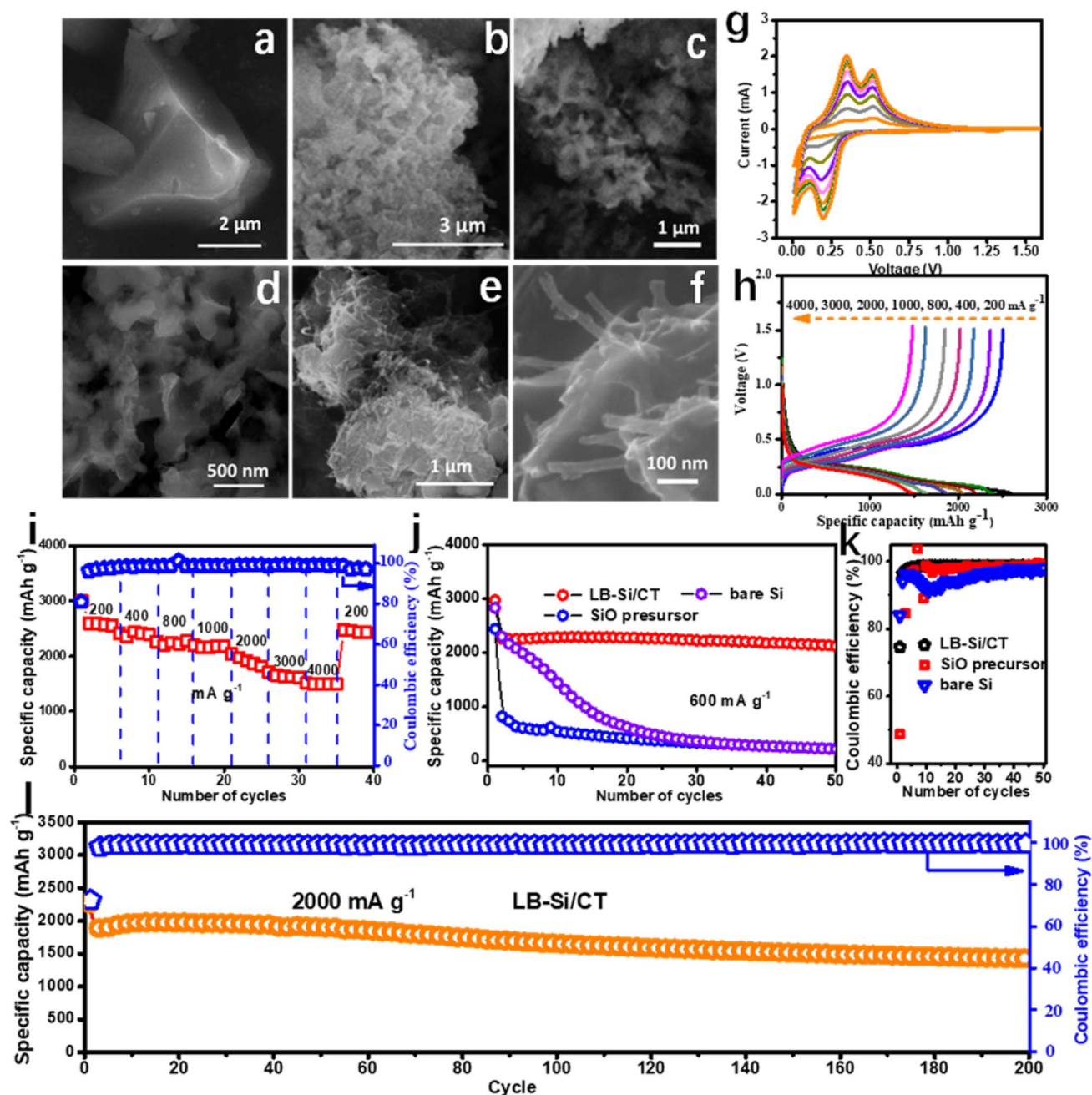
Fig. 2 Scanning electron microscopy images of (a) the SiO precursor, (b–d) LB-Si and (e and f) LB-Si/CT. (g) Cyclic voltammetry curves of the LB-Si/CT electrode *vs.* Li/Li$^+$ at a rate of 0.1 mV s^{-1} from 0.01 to 1.5 V. (h and i) Charge–discharge performance of LB-Si/CT at various current densities. (j) Cycling performance of LB-Si/CT, bare silicon, and the SiO precursor at a current density of 600 mA g^{-1} and (k) corresponding initial coulombic efficiencies. (l) Long cycling performance of LB-Si/CT at 2000 mA g^{-1}.

a relatively low voltage (∼0.1 V), and it provides an initial lithiation specific capacity of 2325.7 mA h g^{-1} and delithiation specific capacity of 2873.3 mA h g^{-1}, indicating a coulombic efficiency is 80.9%. The gradually increasing peak intensity suggests the presence of residual crystalline silicon in the silicon particles, which is a common phenomenon for micro-sized silicon anodes. In addition, the resultant LB-Si/CT composite also exhibits excellent rate capability at various current densities (Fig. 2h–i). Specifically, capacities of 2545,

2446, 2252, 2168, 1864, 1641, and 1498 mA h g^{-1} can be delivered at 200, 400, 800, 1000, 2000, 3000, and 4000 mA g^{-1}, respectively, which are much higher than those of previously reported silicon-based anodes (Fig. S2†).

The cycling performance of LB-Si/CT, bare silicon, and the SiO precursor was further analyzed in the range of 0.01 to 1.5 V at 600 mA g^{-1}, and the results are depicted in Fig. 2j. Apparently, bare silicon suffered severe pulverization and capacity fading, while low lithium storage capacity could be a significant

drawback of SiO. In Fig. 2k, the SiO precursor exhibits a low ICE of 48.7% because of the low electron conductivity and the formation of Li_2O and lithium silicates during the first cycle.[26] Although the initial coulombic efficiency of bare silicon (83.8%) is higher than that of LB-Si/CT (74.5%), its poor structural integrity still deteriorates the stability of the electrode. As shown in Fig. 2l, further examination of deep cycling at 2000 mA g^{-1} gives a high specific capacity of 1426 mA h g^{-1} even after 200 cycles, demonstrating its good structural durability.

The differential capacity analysis of the cathodic peak ($\sim$0.2 V) during deep cycling is presented in Fig. 3a and b. Notably, the magnitude (Fig. 3a) and position (Fig. 3b) of the LB-Si/CT peaks do not significantly change compared with those of bare silicon and the SiO precursor, which suggests a satisfactory structure preservation and electrochemical stability.[27] The galvanostatic intermittent titration technique (GITT) test (Fig. S3†) was further performed at a pulse current of 100 mA g^{-1} for 30 min alternating with 2 h rest intervals to analyze the kinetics of the lithiation process (Fig. S4†). The diffusion coefficient of LB-Si/CT shows a "W"-type pattern (Fig. 3c), which is much higher than that of bare silicon owing to the rational and facile

structural optimization.[28] In addition, the two minimum regions could be originated from the formation of Li_7Si_3 and $Li_{13}Si_4$. Furthermore, the CV curves of LB-Si/CT at various scan rates are presented in Fig. 3d, in which the relationship between the peak current (i) and scan rate (v) could be expressed as $i = av^b$, where a and b could be determined from the intercept and slope of the plot of $\log(i)$ *vs.* $\log(v)$.[29] When the parameter $b = 0.5$, the capacity is dominated by solid-state diffusion, whereas $b = 1$ indicates that the lithium storage is controlled by the surface capacitance.[30] The value of b calculated from the anodic peak is 0.68 (Fig. S5a†), indicating a diffusion-dominated lithium storage mechanism.

To explicitly distinguish the contributions of the diffusion and capacitance, the current response i can be separated into two parts according to the equation $i = k_1v + k_2v^{1/2}$, where k_1v is related to the capacitive process and $k_2v^{1/2}$ corresponds to the diffusion-controlled charge.[31] The capacitive contribution represents 30.4% of the total charge, while the diffusion-controlled contribution dominates the Li-ion storage process (Fig. S5b†). Fig. S6† exhibits the differences between LB-Si/CT, bare silicon, and the SiO precursor before and after cycling.
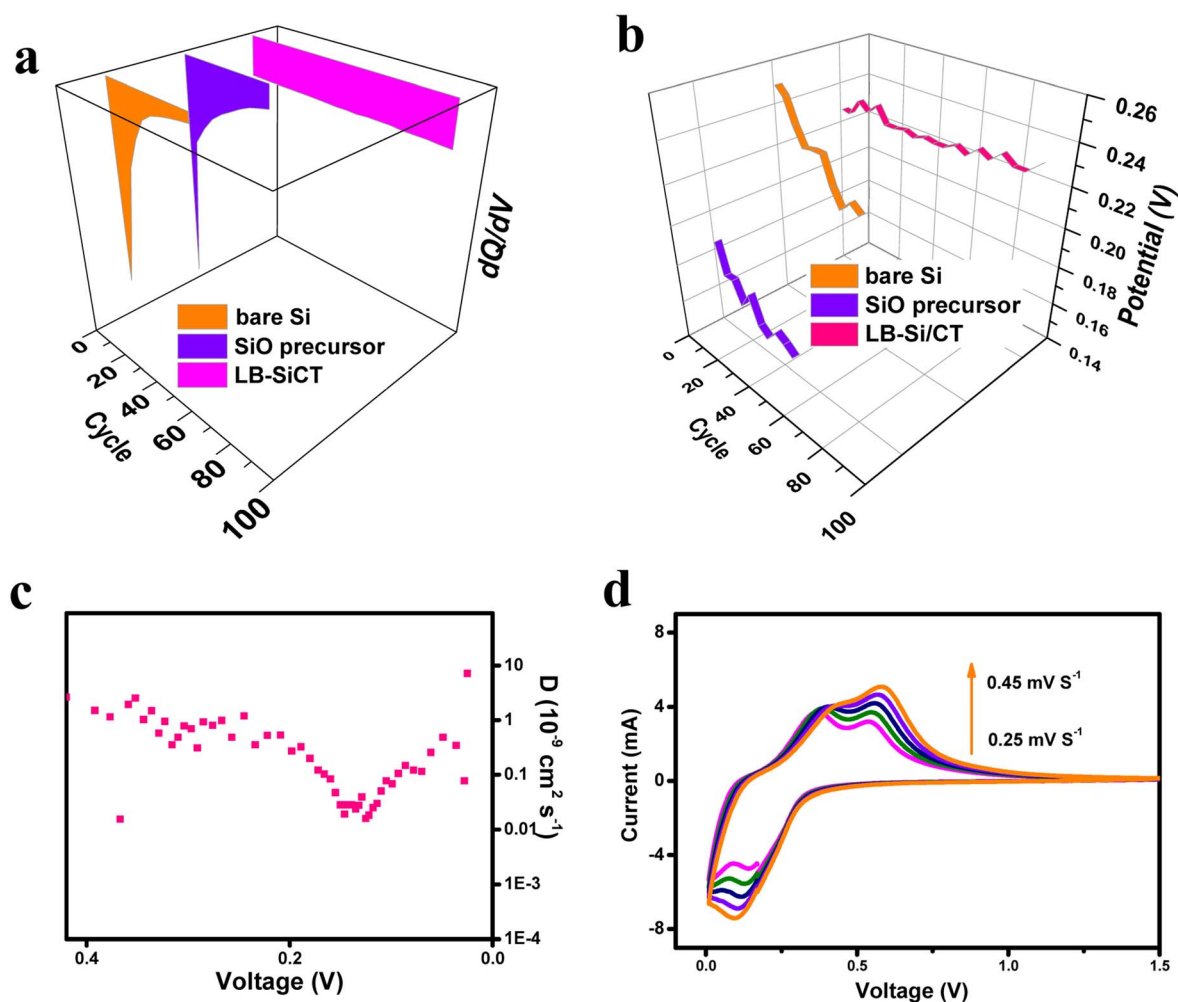

Fig. 3 (a) Differential capacity *vs.* voltage (dQ/dV) cycle curve and (b) potential–cycle curve of the lithiation peak of LB-Si/CT, bare Si, and the SiO precursor. (c) Diffusion coefficient plots and (d) cyclic voltammetry curves at various scan rates from 0.25 to 0.45 mV s^{-1} of LB-Si/CT.

The morphologies of LB-Si/CT before and after cycling are almost the same (Fig. S6a and b†), whereas the electrode integrity of bare silicon and the SiO precursor is significantly compromised, and the copper foil is noticeably exposed (Fig. S6c–f†). These results further confirm that LB-Si/CT effectively relieves the inner mechanical stress during cycling and is therefore suitable for high-energy silicon–graphite electrodes.

Compared with the lithium insertion mechanism in graphite, there is an alloying reaction during the lithium
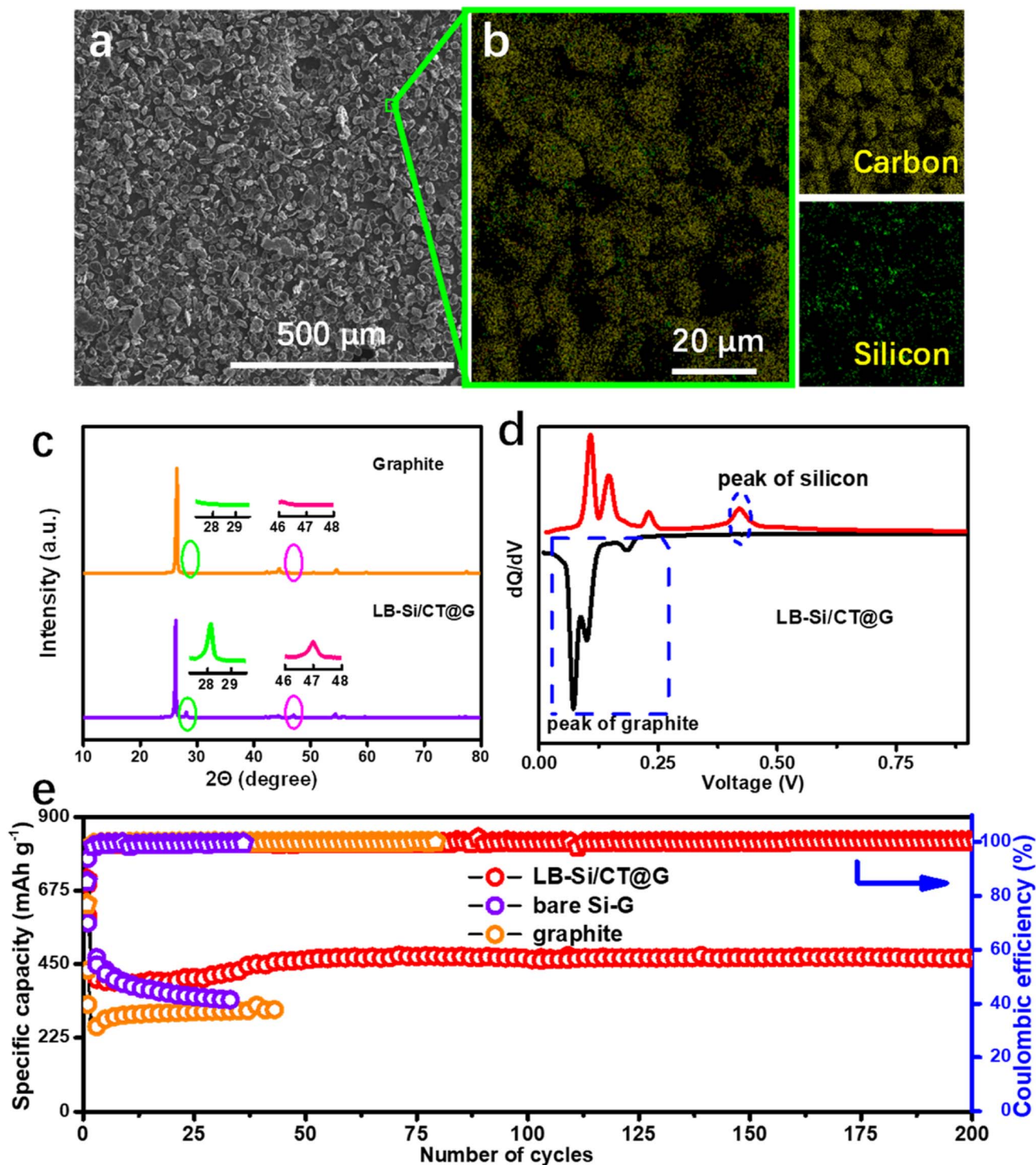

Fig. 4 (a) Scanning electron microscopy images of LB-Si/CT@G and (b) its corresponding energy-dispersive X-ray spectroscopy mapping. (c) X-ray diffraction patterns of graphite and the obtained LB-Si/CT@G. (d) Differential capacity *vs.* voltage plot of the LB-Si/CT@G electrode. (e) Cycling performance of LB-Si/CT@G, the bare Si–G composite, and graphite.

storage process in silicon, leading to a large structural stress. To mitigate the induced stress in silicon, graphite is introduced to further buffer the volume change and promote the stability of the electrode. Fig. 4a and b show the morphology of the as-obtained silicon–graphite electrode (LB-Si/CT@G) and its corresponding energy-dispersive X-ray spectroscopy mapping. A good distribution of silicon is observed in the graphite matrix, and two clear peaks of silicon apart from those of graphite can be clearly identified at around 28° and 47° in the XRD patterns in Fig. 4c.[32] The Raman spectra of graphite, LB-Si/CT and LB-Si/CT@G were recorded and are shown in Fig. S7.† Graphite with a low intensity ratio of the D and G bands (0.38) and silicon with obvious (111) peak reflection can be clearly identified.[33] The differential capacity plots of LB-Si/CT@G during the first cycle were further investigated (Fig. 4d), and lithiation peaks at 0.19, 0.10, and 0.07 V correspond to the following three transformation processes: LiC_{72} to LiC_{36}, LiC_{18} to LiC_{12}, and LiC_{12} to LiC_6, respectively.[34] For the delithiation process, the peaks ascribed to the

deintercalation of graphite (0.11, 0.15, and 0.23 V) and the dealloying of silicon (0.42 V) can also be identified.

The lithiation/delithiation properties of LB-Si/CT@G, bare Si–G, and graphite were further analyzed at 200 mA g^{-1}, and the results are depicted in Fig. 4e. The graphite shows stable cycling durability; however, its capacity is significantly lower than that of LB-Si/CT@G. Due to the volume expansion of bare silicon in the composite, the bare Si–G electrode exhibits unstable lithium storage properties upon deep cycling, which further confirms the necessity of silicon optimization in this work. Moreover, the surface SEM images of LB-Si/CT@G and bare Si–G before and after cycling are depicted in Fig. 5a–f. Obviously, the morphology of LB-Si/CT@G does not change much; however the large volume change of bare silicon in the bare Si–G electrode could break the graphite framework and generate cracks.[35] Differences in the cross-sectional SEM images are also observed in Fig. 5g–j, where the volume change of bare Si–G is much larger than that of LB-Si/CT@G due to the lack of rational structural optimization.
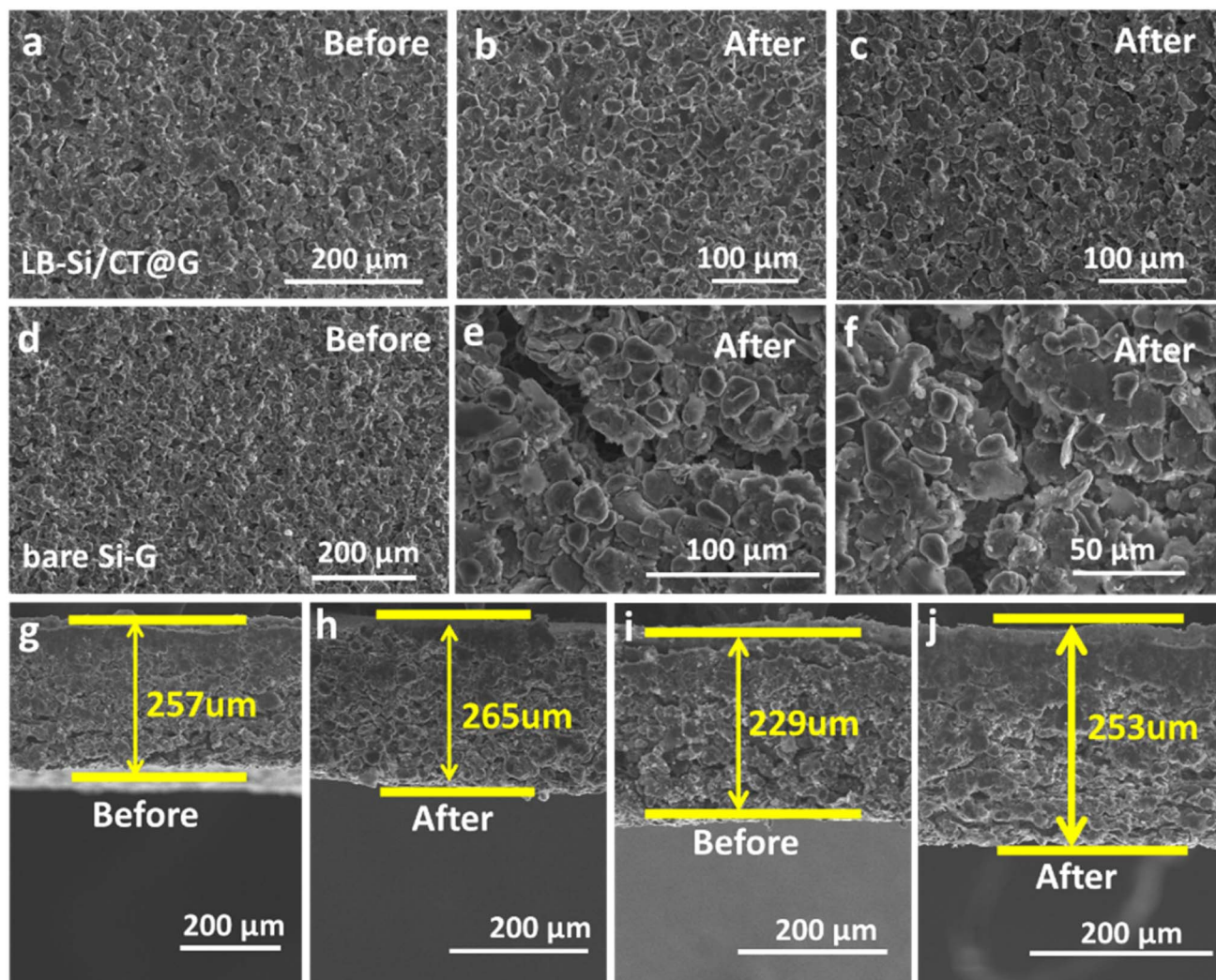

Fig. 5 Scanning electron microscopy (SEM) images of (a–c) LB-Si/CT@G and (d–f) bare Si–G electrodes before and after cycling. Cross-sectional SEM images of (g and h) LB-Si/CT@G and (i and j) bare Si–G before and after cycling.

The charge/discharge performance of the LB-Si/CT@G electrodes with high mass loadings was tested as shown in Fig. 6a. Compared with previous studies, a unique boron modification approach taking advantage of intensive waste heat induced by magnesium reduction is developed. Through thorough mechanical milling, CNTs as conductive agents could be
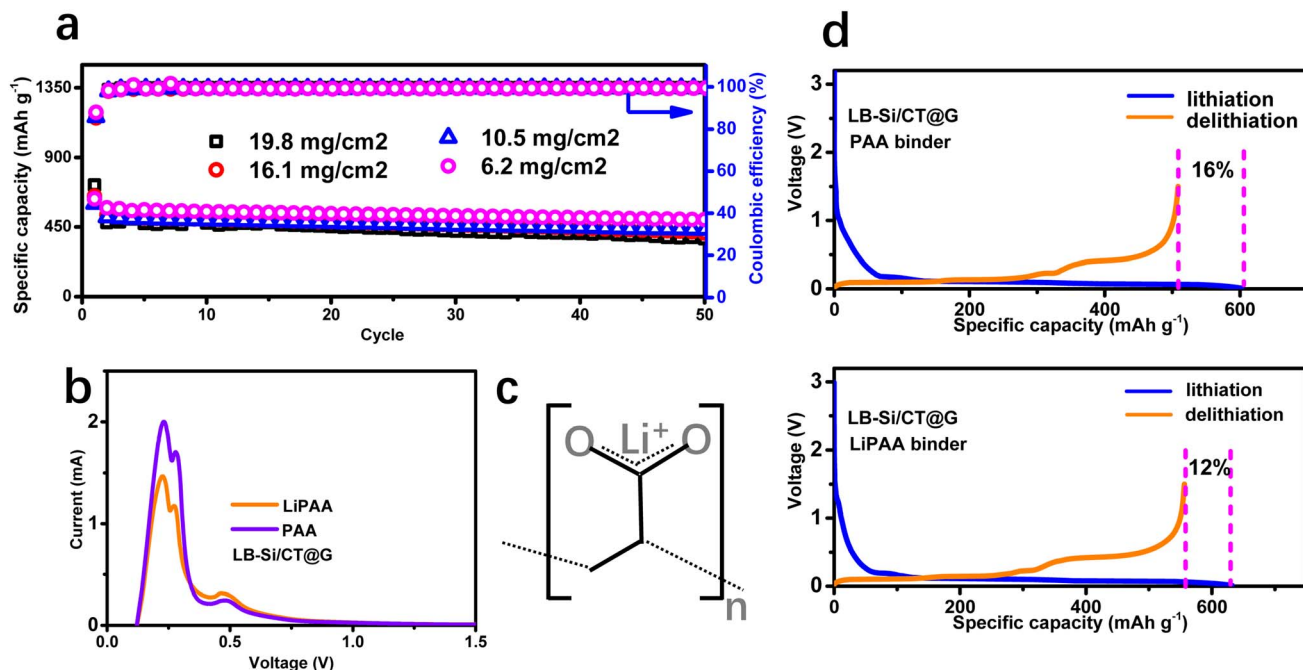

Fig. 6 (a) Charge/discharge performance of the LB-Si/CT@G electrode with different loading amounts. (b) Cyclic voltammetry profiles of LB-Si/CT@G with and without the LiPAA binder. (c) Structure of LiPAA. (d) Initial coulombic efficiency of the LB-Si/CT electrode with the PAA binder and LB-Si/CT@G electrodes with PAA and LiPAA, respectively.
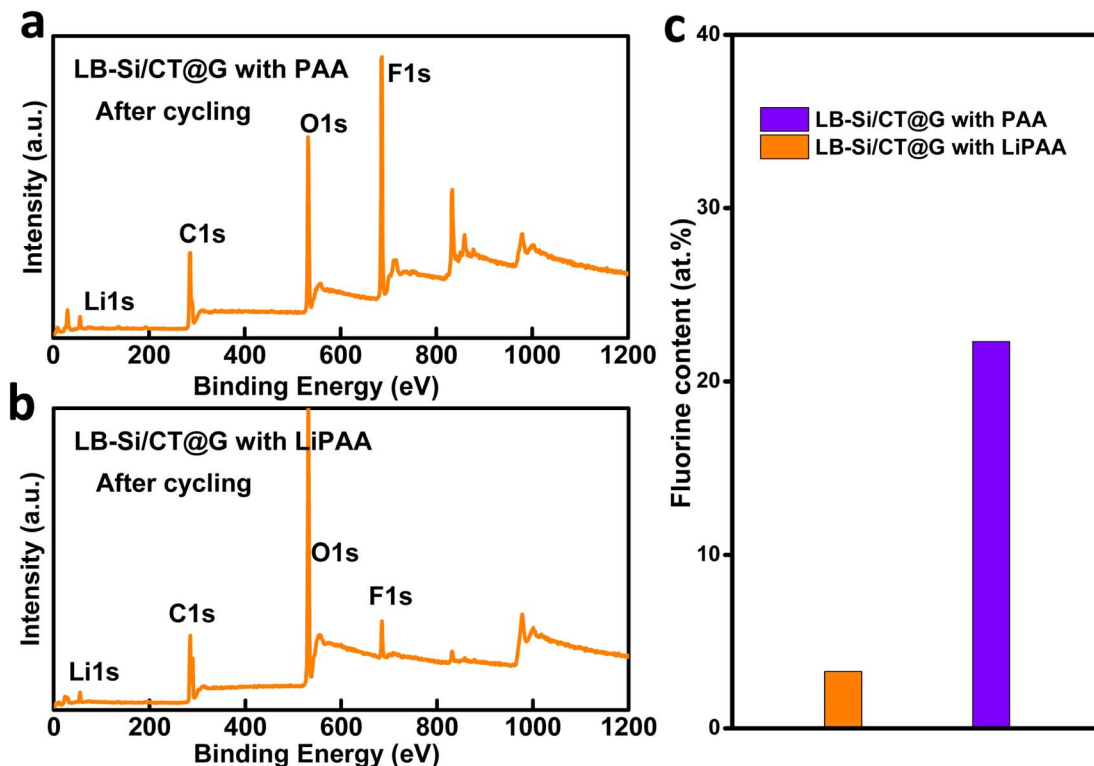

Fig. 7 XPS analysis (a and b) and fluorine content comparison (c) of LB-Si/CT@G with PAA and LiPAA after cycling.

successfully inserted into the pores of silicon particles. The lithium storage capability with ultrahigh electrode loading (19.8 mg cm^{-2}) is another advantageous feature of LB-Si/CT@G, corresponding to a remarkable areal capacity of 7.4 mA h cm^{-2} at a current density of 1.0 mA cm^{-2}. Besides, with rational design, the initial coulombic efficiency could be effectively enhanced to a high level (88%). Thus, the LB-Si/CT@G electrode is highly competitive with other reported silicon-based anodes (Table S1†).

A friction test is further conducted on a Multifunctional Friction Testing Machine (MFT-5000, Rtec, USA). Under a load of 1 N, friction time of 5 min and friction pair of zirconium oxide, the volume abrasion rate of the prepared LB-Si/CT@G electrode (2.47%) is clearly lower than that of pure silicon (3.43%) (Fig. S8†). Finite element simulation is carried out on COMSOL using the partial differential equation method based on the model of silicon surrounded by a layer of the graphite/binder mixture. It could be identified in Fig. S9† that the tangential stress of the silicon–graphite electrode is much lower than that of the comparative silicon electrode at different states of charge (SOC), which further verifies the high stability of the obtained silicon–graphite electrode. Additionally, the engineered lithium-rich binder could also provide a more stable electrode structure during the charge/discharge process (Fig. S10†). In comparison, the oxidation currents of the electrodes with LiPAA are lower than those with polyacrylate (PAA) (Fig. 6b). This indicates that the LiPAA binder could effectively play the role of a physical barrier and mitigate the oxidation of the electrolyte.[36] There are active carboxylate groups in LiPAA that can chemically interact with species present at the particle surface. The oxygen at the surfaces of silicon particles (Fig. S11†) could react with LiPAA to form ester-like bonds, resulting in relatively uniform binder coverage.[36] In addition, LiPAA could affect their interfacial transport properties remarkably, promoting the Li$^+$ ion transport properties of the SEI due to the polymer's intrinsic Li$^+$ ion conducting properties.[37,38]

The GITT test results presented in Fig. S12† suggest an improved diffusion coefficient and enhanced lithium transfer behavior of the electrode with the lithium-rich binder (Fig. 6c).[40,41] The Li-ion conducting film also acts as a buffer interphase that prevents detrimental surface reactions and the formation of resistive surface species. The LiPAA based electrode could provide a higher initial coulombic efficiency (Fig. 6d).[39] To further understand the effect of LiPAA on the surface chemical properties of the electrodes, we conducted XPS analysis. Compared with the pristine electrode (Fig. S13a and b†), fluorine and lithium emerge in the anode surface after cycling, as shown in Fig. 7. According to the significantly lower fluorine content (3.3 at%) after cycling (Fig. 7), it could be concluded that LB-Si/CT@G with LiPAA has weaker surface electrolyte decomposition and lithium salt reduction induced by mediated intermolecular hydrogen-bonding strength than the electrode with PAA.[42–44]

Conclusions

In summary, we propose a facile solid-state strategy to overcome the limitations of silicon-based anodes, namely, tedious silicon optimization, unsatisfactory ICE, low electrode loading level and insufficient areal capacity. The strategy takes advantage of magnesium reduction as well as its intensive waste heat for porosity construction and boron doping, lithium-rich binder engineering and incorporation of a reliable graphite framework. As expected, the modified LB-Si/CT active material exhibits a high specific capacity of 2585 mA h g^{-1} and excellent cycling durability over 200 cycles. After graphite incorporation, the LB-Si/CT@G electrode achieves an ultrahigh loading level of $\sim$20 mg cm^{-2} and impressive areal capacity of 7.4 mA h cm^{-2}. This study provides a low-cost, facile alternative for high-energy-density lithium-ion batteries, which is also applicable to other high-performance nano/micro-materials for next-generation energy storage devices.

Conflicts of interest

There are no conflicts to declare.

Acknowledgements

Notes and references

1 Y.-K. Sun, Z. H. Chen, H. J. Noh, D. J. Lee, H. G. Jung, Y. Ren, S. Wang, C. S. Yoon, S. T. Myung and K. Amine, *Nat. Mater.*, 2012, **11**, 942.

2 B. Scrosati, J. Hassoun and Y.-K. Sun, *Energy Environ. Sci.*, 2011, **4**, 3287.

3 Y.-K. Sun, S. T. Myung, B. C. Park, J. Prakash, I. Belharouak and K. Amine, *Nat. Mater.*, 2009, **8**, 320.

4 C. K. Chan, H. L. Peng, G. Liu, K. McIlwrath, X. F. Zhang, R. A. Huggins and Y. Cui, *Nat. Nanotechnol.*, 2008, **3**, 31.

5 W. M. Zhang, J. S. Hu, Y. G. Guo, S. F. Zheng, L. S. Zhong, W. G. Song and L. J. Wan, *Adv. Mater.*, 2008, **20**, 1160.

6 T. Kennedy, E. Mullane, H. Geaney, M. Osiak, C. O'Dwyer and K. M. Ryan, *Nano Lett.*, 2014, **14**, 716.

7 B. Zhu, X. Y. Wang, P. C. Yao, J. L. Li and J. Zhu, *Chem. Sci.*, 2019, **10**, 7132.

8 M. Y. Ge, J. P. Rong, X. Fang, A. Y. Zhang, Y. H. Lu and C. W. Zhou, *Nano Res.*, 2013, **6**, 174.

9 R. Yi, J. T. Zai, F. Dai, M. L. Gordin and D. H. Wang, *Electrochem. Commun.*, 2013, **36**, 29.

10 R. Yi, F. Dai, M. L. Gordin, S. R. Chen and D. H. Wang, *Adv. Energy Mater.*, 2013, **3**, 295.

11 M. W. Forney, M. J. Ganter, J. W. Staub, R. D. Ridgley and B. J. Landi, *Nano Lett.*, 2013, **13**, 4158.

12 P. Li, J.-Y. Hwang and Y.-K. Sun, *ACS Nano*, 2019, **13**, 2624.

13 Y. Yan, Y. X. Yin, S. Xin, J. Su, Y. G. Guo and L. J. Wan, *Electrochim. Acta*, 2013, **91**, 58.

14 F. Z. Zhang, G. J. Zhu, K. Wang, X. Y. Qian, Y. Y. Zhao, W. Luo and J. P. Yang, *J. Mater. Chem. A*, 2019, **7**, 17426.

15 J. Y. Wang, L. Liao, H. R. Lee, F. F. Shi, W. Huang, J. Zhao, A. Pei, J. Tang, X. L. Zheng, W. Chen and Y. Cui, *Nano Energy*, 2019, **61**, 404.

16 Y. He, X. Q. Yu, Y. H. Wang, H. Li and X. J. Huang, *Adv. Mater.*, 2011, **23**, 4938.

17 S. Hitomi, K. Kubota, T. Horiba, K. Hida, T. Matsuyama, H. Oji, S. Yasuno and S. Komaba, *ChemElectroChem*, 2019, **6**, 5070.

18 T. Lu and Q. Chen, *Theor. Chem. Acc.*, 2020, **139**, 25.

19 S. Zhang, G. Wang, B. Wang, J. Wang, J. Bai and H. Wang, *Adv. Funct. Mater.*, 2020, **30**, 2001592.

20 M. Chen, B. Li, X. J. Liu, L. Zhou, L. Yao, J. T. Zai, X. F. Qian and X. B. Yu, *J. Mater. Chem. A*, 2018, **6**, 3022.

21 P. Li, J.-Y. Hwang, S. M. Park and Y.-K. Sun, *J. Mater. Chem. A*, 2018, **6**, 12551.

22 R. Yi, S. R. Chen, J. X. Song, M. L. Gordin, A. Manivannan and D. H. Wang, *Adv. Funct. Mater.*, 2014, **24**, 7433.

23 P. Li, J. Y. Liu, Y. Liu, Y. W. Wang, Z. T. Li, W. T. Wu, Y. Wang, L. H. Yin, H. Xie, M. B. Wu, X. J. He and J. S. Qiu, *Electrochim. Acta*, 2015, **180**, 164.

24 X. L. Li, P. F. Yan, X. C. Xiao, J. H. Woo, C. M. Wang, J. Liua and J. G. Zhang, *Energy Environ. Sci.*, 2017, **10**, 1427.

25 S. S. Zhu, J. B. Zhou, Y. Guan, W. L. Cai, Y. Y. Zhao, Y. C. Zhu, L. Q. Zhu, Y. C. Zhu and Y. T. Qian, *Small*, 2018, **14**, 1802457.

26 M. Miyachi, H. Yamamoto and H. Kawai, *J. Electrochem. Soc.*, 2007, **154**, A376.

27 A. Ulvestad, H. F. Andersen, I. J. T. Jensen, T. T. Mongstad, J. P. Maehlen, O. Prytz and M. Kirkengen, *Sci. Rep.*, 2018, **8**, 8634.

28 N. Ding, J. Xu, Y. X. Yao, G. Wegner, X. Fang, C. H. Chen and I. Lieberwirth, *Solid State Ionics*, 2009, **180**, 222.

29 V. Augustyn, J. Come, M. A. Lowe, J. W. Kim, P. L. Taberna, S. H. Tolbert, H. D. Abruna, P. Simon and B. Dunn, *Nat. Mater.*, 2013, **12**, 518.

30 P. Li, J.-Y. Hwang and Y.-K. Sun, *J. Mater. Chem. A*, 2019, **7**, 20675.

31 W. Tian, H. Hu, Y. X. Wang, P. Li, J. Y. Liu, J. L. Liu, X. B. Wang, X. D. Xu, Z. T. Li, Q. S. Zhao, H. Ning, W. T. Wu and M. B. Wu, *ACS Nano*, 2018, **12**, 1990.

32 J. X. Li, Z. B. Li, W. J. Huang, L. Chen, F. C. Lv, M. Z. Zou, F. Qian, Z. G. Huang, J. Lu and Y. Y. Li, *Small*, 2019, **15**, 1900436.

33 P. Nie, Z. Y. Le, G. Chen, D. Liu, X. Y. Liu, H. B. Wu, P. C. Xu, X. R. Li, F. Liu, L. M. Chang, X. G. Zhang and Y. F. Lu, *Small*, 2018, **14**, 1800635.

34 M. Sohn, D. G. Lee, H. I. Park, C. Park, J. H. Choi and H. Kim, *Adv. Funct. Mater.*, 2018, **28**, 1800855.

35 P.-K. Lee, M. H. Tahmasebi, S. Ran, S. T. Boles and D. Y. W. Yu, *Small*, 2018, **14**, 1802051.

36 N. P. W. Pieczonka, V. Borgel, B. Ziv, N. Leifer, V. Dargel, D. Aurbach, J. H. Kim, Z. Y. Liu, X. S. Huang, S. A. Krachkovskiy, G. R. Goward, I. Halalay, B. R. Powell and A. Manthiram, *Adv. Energy Mater.*, 2015, **5**, 1501008.

37 J. Li, D. B. Le, P. P. Ferguson and J. R. Dahn, *Electrochim. Acta*, 2010, **55**, 2991.

38 J. Chong, S. Xun, H. Zheng, X. Song, G. Liu, P. Ridgway, J. Q. Wang and V. S. Battaglia, *J. Power Sources*, 2011, **196**, 7707.

39 W. Porcher, S. Chazelle, A. Boulineau, N. Mariage, J. P. Alper, T. Van Rompaey, J.-S. Bridel and C. Haon, *J. Electrochem. Soc.*, 2017, **164**, A3633.

40 K. A. Hays, R. E. Ruther, A. J. Kukay, P. F. Cao, T. Saito, D. L. Wood and J. L. Li, *J. Power Sources*, 2018, **384**, 136.

41 A. Y. Su, Q. Pang, X. Chen, J. J. Dong, Y. Y. Zhao, R. Q. Lian, D. Zhang, B. B. Liu, G. Chen and Y. J. Wei, *J. Mater. Chem. A*, 2018, **6**, 23357.

42 P. Parikh, M. Sina, A. Banerjee, X. F. Wang, M. S. D'Souza, J. M. Doux, E. A. Wu, O. Y. Trieu, Y. B. Gong, Q. Zhou, K. Snyder and Y. S. Meng, *Chem. Mater.*, 2019, **31**, 2535.

43 U. S. Vogl, S. F. Lux, E. J. Crumlin, Z. Liu, L. Terborg, M. Winter and R. Kostecki, *J. Electrochem. Soc.*, 2015, **162**, A603.

44 T. Jaumann, J. Balach, M. Klose, S. Oswald, U. Langklotz, A. Michaelis, J. Eckerta and L. Giebelera, *Phys. Chem. Chem. Phys.*, 2015, **17**, 24956.